Ultraviolet HST Snapshot Survey of 3CR Radio Source Counterparts at Low Redshift

Mark G. Allen[1], William B. Sparks[1], Anton Koekemoer[1], Andre R. Martel[2], Christopher P. O'Dea[1], Stefi A. Baum[1], Marco Chiaberge[1], F. Duccio Macchetto[1], George K. Miley[3]

ABSTRACT

We present ultraviolet images of 27 3CR radio galaxies with redshifts $z <0.1$ that have been imaged with the *Space Telescope Imaging Spectrograph (STIS)* on board the *Hubble Space Telescope (HST)*. The observations employed the NUV-MAMA and broad-band filters with peak sensitivity at 2200Å. We find that the UV luminosities show approximately a factor of 10 to 100 higher dispersion than the optical. We compare the UV morphologies with optical *V*- and *R*-band WFPC2 snapshot survey images. We have found dramatic, complex and extended ultraviolet emission from radio galaxies *even at zero redshift*. We find a diverse range of UV morphologies, some completely divergent from their visual morphology, which are reminiscent of the chaotic high-z radio galaxies structures seen in rest-frame UV. The UV morphologies show regions of star formation, jets, and possible scattered AGN continuum. The UV emission is generally not aligned with the radio structure. We also detect the diffuse UV emission of the host galaxy. We propose that these are the same physical phenomena as observed at high redshift, but on a smaller spatial scale.

Subject headings: galaxies: elliptical and lenticular, cD — galaxies: evolution — galaxies: jets — galaxies: nuclei — ultraviolet: galaxies — surveys

1. Introduction

The study of radio galaxies impacts many areas of astrophysics and cosmology. Typically the hosts of powerful radio sources are massive, early-type elliptical galaxies that often lie at the heart of clusters (Matthews, Morgan and Schmidt 1964; Yates, Miller, & Peacock 1989; Zirbel 1996; Hill & Lilly 1991). How these galaxies and clusters are assembled in the early universe from

---

[1]Space Telescope Science Institute, Baltimore, MD 21218

[2]Department of Physics and Astronomy, Johns Hopkins University, 3400 N. Charles Street, Baltimore, MD 21218

[3]Leiden Observatory, P.O. Box 9513, NL-2300 RA Leiden, The Netherlands

the initial fluctuations is largely unknown. The detailed physics of mergers, competing cooling and heating processes and gravitational aggregation that leads to the massive clusters and giant dominant central galaxies are currently poorly understood.

Radio galaxies can be seen at all redshifts, thus providing an important, consistent probe whose systematic characteristics may be traced from the earliest observable times to the present. Not only that, but the fact that they are massive evolving galaxies, often in a most privileged position at the sites of cosmological structure formation, makes them especially important in achieving an accurate picture of the physics and evolution of the universe.

While the relationship between AGN evolution and galaxy evolution is unknown, there may be links between radio galaxy activity and star formation (Dey, van Breugel, Vacca, & Antonucci 1997; Bicknell et al. 2000) . The epoch of intense star formation in the universe is similar to the period when the volume density of quasars and radio galaxies was orders of magnitude higher than it is today. Recent X-ray observations show directly that the radio sources themselves interact perhaps in a fundamental way with the hot coronal intra-cluster gas (Smith et al. 2001; Hardcastle, Birkinshaw, & Worrall 2001) that represents one of the most massive cluster components after the dark matter.

Black hole searches have shown that almost every large elliptical galaxy harbors a massive black hole (Magorrian et al. 1998; Ferrarese & Merritt 2000), implying all such galaxies go through an active phase. The ubiquity of activity in galaxies thus makes the study of radio galaxies crucial for galaxy evolution and understanding how this phase affects the star formation, gas and dust content, and dynamics of the host galaxy. Investigation of the nuclear environments of radio galaxies is an important area of AGN physics research, with implications for the triggering, fueling and evolution of the active nucleus.

At high redshift ($z > 0.6$) the UV rest frame continua of radio galaxies are closely aligned with their radio sources (McCarthy et al. 1987; Chambers et al. 1987). The alignment effect implies that the radio source may play a fundamental role in the evolution of the galaxy and clusters of galaxies. The orientations of lower redshift and lower luminosity radio galaxies have been studied in detail with claims of both minor and major axis alignments with respect to the radio lobes (Baum and Heckman 1989).

These processes have been well studied at optical wavelengths via the 3CR Imaging Snapshot Surveys conducted with *Hubble Space Telescope* (HST) in Cycles 4-8. Nearly all the extragalactic radio sources in the 3CR catalog (Bennett 1962a,b; Spinrad et al. 1985) were observed in this series of programs. Impressive results concerning the prevalence of dust disks and optical jets are described in Martel et al. (1998, 1999); Lehnert et al. (1999); McCarthy et al. (1997); de Koff et al. (1996).

Here we describe an observational program to obtain high spatial resolution HST UV images of nearby powerful 3CR radio galaxies. We present the results of UV imaging of the low redshift ($z < 0.1$) subset of the sample. These UV images are a major enhancement to the existing database,

and represent the first systematic high spatial resolution survey of radio galaxies in this unexplored spectral window. In particular, using UV imaging we seek to distinguish the relative roles of gas, dust, jets and star formation at the present time. The UV band is well suited to addressing these questions because of the high sensitivity to the youngest, hottest stars, and blue synchrotron jets. Also the UV is optimal for detecting scattered emission because of the blue colour of the illuminating nuclei, and the high efficiency of scattering at shorter wavelengths.

A primary motivation for UV imaging of these nearby 3CR sources is to provide a zero redshift comparison sample for the extraordinary rest frame UV morphologies found at high redshift. In any systematic study spanning a significant fraction of the age of the universe it is difficult to disentangle the effects of evolution, intrinsic power and wavelength of the observation. For the first time we can empirically characterize the rest frame UV structure of radio galaxies at zero redshift.

The details of the observations and data processing are described in § 2. The UV fluxes and extinction-corrected luminosities of all the objects are presented in § 3 along with descriptions of the individual sources and their corresponding optical and radio properties. In § 4 the UV and optical luminosities are compared to predictions from star formation and and ionized gas emission models. Discussion is presented in § 5

2. Observations and Processing

Table 1 lists the dates and exposure times of the UV snapshot observations. All the UV snapshot observations employed the STIS Near Ultraviolet (NUV) Cs_2Te Multi-Anode Microchannel Array (MAMA) detector. This detector has a field of view of 25×25 arcsec^2, and a pixel size of ~ 0.024 arcseconds. Most of the objects were observed with the F25SRF2 filter, and in number of cases the narrower band F25CN182 filter was used due to the bright object limits of the NUV-MAMA. The F25SRF2 filter provides a transmission function a central wavelength of 2320Å and FWHM of 1010Å . The short wavelength cutoff excludes Geocoronal Lyman-α 1216Å emission. The F25CN182 filter provides medium band width imaging with pivot wavelength of 1983Å with a FWHM of 630Å .

All the images were processed through the HST pipeline calibration. The flux calibration of the pipeline is expected to be accurate to 5%. We use the pipeline provided zero-points given by the values of the PHOTFLAM header keywords which were 5.619×10^{-18} for F25SRF2 and 6.144×10^{-17} for F25CN182 in units of ergs cm^{-2} Å^{-1}. That is the flux in ergs s^{-1} cm^{-2} Å^{-1} is obtained by multiplying PHOTFLAM by the observed countrate.

For the 14 objects in our sample with redshift greater than z= 0.05 the F25SRF2 filter will include any rest frame Lyman-α 1216Å emission. Using IRAF synphot calculations with the assumption of a strong emission line spectrum (NGC 1068) we find that Lyman-α can contribute up to 9% of the total flux in the F25SRF2 bandpass for these objects.

The images were rotated to a North up, East left orientation. The IRAF *drizzle* package was used to apply the rotation and image shifts. The drizzle procedure output sampling was the same as the input sampling, which leads to slight smoothing of the image compared to the raw data. The benefit of using drizzle is that the flux is preserved, and the loss of resolution is minimized.

The astrometry reported in the image header files is typically mismatched by up to ~ 1 arcsecond with respect to the WFPC2 image of the same object. In order to register the NUV-MAMA image with the WFPC2 image we applied a shift to the NUV-MAMA image and used the WFPC2 astrometry. In cases with a bright point source common to both WFPC2 and NUV-MAMA images a shift was applied to register on the point source. In other cases the shift was applied to register common extended image structures. The details of the registrations applied to each case are described in the notes on the individual objects. For the present purposes the absolute accuracy of the astrometry is not important.

Note that in the bright nuclear dominated UV images there is a ghost image offset $\sim 1.2''$ to the left of the object (in the original unrotated STIS images). This is most likely due to a refection within the STIS instrument.

2.1. Background Level and Flux Estimation

For each object we have measured the total UV and optical emission. This was done using a set of masks which were defined individually for each galaxy. Since the images at different wavelengths were registered spatially and onto the same scale, as described above, we use the same suite of masks for the optical images as well as the UV images.

In order to measure the total UV emission it is first necessary to estimate the UV background level. The great majority of targets appear to be confined within the extent of the 25×25 arcsec^{-2} field of view, although a few show structure extending to the edges of the frame. Additionally, the NUV MAMA detector has an instrumental effect of enhanced (dark current) signal around the edges of the detector, see Figure 1. To estimate the background countrate, therefore, we defined a circular aperture of 800 pixels diameter centered on the MAMA and excluded the regions of the image exterior to that circle. Next, we identified the region of source emission by heavily smoothing the image with a $\sigma = 21$ Gaussian kernel, then thresholding to a level of 0.1 counts above the background (Figure 2). This corresponds to the level at which diffuse source emission is starting to become comparable to the enhanced dark current around the detector edges, see Figure 1. The corresponding surface brightness of this minimum detectable diffuse emission is 6.7×10^{-19} ergs s^{-1} cm^{-2} Å^{-1}arcsec^{-2} for the F25SRF2 filter (the most commonly used) and 7.3×10^{-18} ergs s^{-1} cm^{-2} Å^{-1}arcsec^{-2} for the lower throughput F25CN182 filter. The background countrate was then estimated as the average value exterior to the source defined in this way, and interior to the detector edge mask. To measure the total UV emission, we summed the counts within the source region, subtracted the estimated background and applied the appropriate photometric

conversion as described above.

It is possible that there is a contribution of diffuse extended UV source emission across the field of view at a surface brightness below this level. Figure 3 shows the derived countrates for all the sources. Sky background on the day side of the orbit contains a significant contributions from OII air glow emission at 2470Å and OI air glow at 1302Å . In high-background conditions, the sky background can dominate the detector background. In average day-side observing conditions about half the background will be from the sky and half from detector dark current. A typical detector plus sky background level to be expected is $\sim 1.0 \times 10^{-3}$ counts s^{-1} pixel^{-1}, with a range $\sim 0.8 \times 10^{-3}$ counts s^{-1} pixel^{-1} to $\sim 1.7 \times 10^{-3}$ counts s^{-1} pixel^{-1}. As noted above, the STIS pipeline subtracts an estimate of the detector background, intended to leave sky and source. The residual background (ie. dark subtracted) levels we estimate have a median and standard deviation of 0.37×10^{-3} counts s^{-1} pixel^{-1} and 0.49×10^{-3} counts s^{-1} pixel^{-1} respectively. The residual background shows no correlation with the pipeline subtracted dark (see Figure 4). The sky level is expected to be in the range 6.25×10^{-6} to 1.2×10^{-3} counts s^{-1} pixel^{-1}. As shown in the histogram of background countrates, Figure 5, all but three of our residual background measurements are within this range.

In the optical data, there certainly is a contribution of galaxy emission within the UV background region. We recorded that level also in order to make color measurements, and return to this in § 5.1. In Figure 4 we plot the derived UV background versus total UV flux in order to assess the likely contribution of large scale diffuse emission. The lack of any correlation here suggests that such diffuse emission does not dominate our flux estimates, with the possible exception of 3C 231 (M 82) where the source fills the entire field of view.

In Table 2 the redshift, radio properties, and galactic reddening values for each object are tabulated.

3. RESULTS

3.1. Quantitative UV, Optical and Radio properties

Table 3 lists the measurements of the total UV fluxes in units of F_λ(erg s^{-1} cm^{-2} Å^{-1}) for all the objects in the sample. In addition we include the corresponding F702W and F555W fluxes extracted from the same aperture mask. Note that these raw flux measurements have not been corrected for galactic reddening. In Table 4 we list the total UV, F702W and F555W luminosities. These luminosities were converted from the flux measurements using the distance derived from the redshift (H$_0$ = 75 km s^{-1} Mpc^{-1}) and the filter bandwidth as specified by the PHOTBW header keywords. The Luminosities also include a correction for galactic reddening. The reddening corrections were calculated using the $E(B-V)$ values from Schlegel, Finkbeiner, & Davis (1998) (provided via NED for each individual object's sky position) and the reddening curve of Cardelli,

Clayton, & Mathis (1989) as included in SYNPHOT. To determine reddening correction factors to the F25SRF2, F25CN182, F702W and F555W fluxes of each object we used synphot to calculate the inverse transmission of a flat spectrum with reddening applied with the ebmvx function.

3.2. Description of Individual Sources

In Figures 7 to 33 we compare the UV and optical images of the sample. In all the images presented in this section the RA and DEC coordinate axes are based on the astrometry reported in the WFPC2 F702W or F555W filter images from the optical snapshot survey. The coordinates have been precessed to the B1950.0 epoch to facilitate comparisons with published radio maps, and to provide consistency with the coordinates shown for the same F702W images published in Martel et al. (1999). In each UV image we also include a bar in the upper right corner which indicates the direction of the radio jet axis, and a scale bar labeled in kpc is included in the lower right corner.

3C 29

The UV image of this galaxy is presented in Figure 7a, and has been smoothed by a Gaussian with a FWHM of 3 pixels. The F702W image of this galaxy, shown in Figures 7b shows a very round and smooth light distribution, with a relatively faint compact nucleus. At higher contrast a distorted X-shaped dust lane is visible. This is seen more clearly in the F555W image and in more detail in Sparks et al. (2000). The two filaments that cross to form the X, intersect at the nucleus of the galaxy and extend approximately $1''$ out from the nucleus. We note that the linear feature positioned $\sim 2''$ NW of the nucleus in the F702W image published in Martel et al. (1999) is an image processing artifact. The UV image consists of faint extended galaxy emission, visible out to a $2''$ radius, and the compact nucleus is detected. The UV image shows no evidence of the X-shaped dust feature although this is likely due to the relatively low signal to noise of this observation. This image represents the first detection of this object in the UV as it was undetected with the FOC observation of (Zirbel and Baum 1998). Neither the optical nor UV emission show any relation to the radio jet axis.

3C 35

The UV image of this galaxy is presented in Figure 8a and has been smoothed by a Gaussian with a FWHM of 3 pixels in order to improve the signal to noise of this faint source. The smoothed image shows a faint compact nucleus surrounded by some very low level diffuse emission. There is some indication of extended emission extending $\sim 1''$ south of the nucleus, roughly in the direction of the radio jet. There is no indication of such an extended structure in the optical image (Figure 8b). The asymmetry of optical light distribution is due to a $0.5''$ scale dust lane which curves around the northern edge of the source. Note that the radio axis is perpendicular to the dust lane.

3C 40

The UV image of this galaxy is shown in Figure 9a, and has been smoothed by a Gaussian with

FWHM of 3 pixels. The UV image reveals diffuse emission over a scale of $3''$. The central region displays a well defined $2''$ diameter half-circle of extinction. The straight edge of the half-circle bisects a weak UV nucleus. The UV morphology is well matched to the scale of the elongated dust disk seen in the optical image (Figure 9b). (Note that the object is located at the edge of the WF4 chip in the F702W image.) The UV emission is somewhat irregular in the northern half of the disk, but there is no apparent relationship to the radio jet axis.

3C 66B

The UV image of this galaxy is shown in Figure 10a, and has been smoothed by a Gaussian with FWHM of 3 pixels. It reveals a strong collimated jet of UV emission aligned along the direction of radio axis. The prominent jet extends up to $10''$ from the nucleus and UV emission is detected continuously along the whole length of the jet. A strong knot, or kink in the jet occurs at a distance of $3''$ from the nucleus, after which the jet flares and remains more diffuse. The jet is faintly visible in the F702W image (Figure 10b) and also in F555W and F814W optical images (not shown here). This UV jet is an important addition to the 12 or so optical jets that have been detected in extragalactic radio sources. The close relationship of the UV jet to the radio jet morphology, and its similarity to other known jets clearly indicates that it is synchrotron emission. A detailed analysis will be presented in Sparks et al. (2001). The compact nucleus seen in the optical images is well detected in the UV. The small $1''$ diameter face-on dust disk seen at the centre of the optical images is not apparent in the UV, although the host galaxy emission is visible in the UV images. An additional UV object is detected $\sim 6''$ north of the nucleus. This feature has a faint optical counterpart in the optical images.

3C 192

The UV image of this galaxy is shown in Figure 11a, and has been smoothed by a Gaussian with FWHM of 3 pixels. The UV image displays a compact core surrounded by diffuse UV emission structures. A $1''$ slightly curved arc, or bar of UV emission is seen on the east side of the compact core. A similar slightly larger and more diffuse feature is present $0.5''$ from the core on the opposite side. The lower level diffuse UV emission forms a faint spiral structure that is roughly elongated along the radio jet direction. The diffuse UV spiral emission is similar in morphology to 3C 305, where the shape is clearly determined by dust effects, yet the optical F555W image of 3C 192 shows no counterpart to the diffuse UV emission, nor does it show any evidence for dust. (Note that the F702W image from the WFPC2 snapshot survey was not pointed correctly and the object fell outside the WFPC2 field.)

3C 198

The UV image of this galaxy is shown in Figure 12a. The UV image shows a complex and interesting array of UV emission structures. The relatively bright nucleus is well detected and is surrounded by irregular diffuse emission that has no counterpart in the optical image (Figure 12b). In addition we detect the faint diffuse extended UV emission of the host galaxy, plus 5 or more compact UV sources distributed over $3''$ scale region. None of these features appear to be related

to the radio jet axis. The UV image shows a nucleus, surrounded by irregular diffuse emission and a number of other point like sources which have no optical counterparts. A further UV object is detected $6''$ SW of the nucleus, with a faint counterpart in the optical image.

3C 227

Figure 13a shows the UV image of 3C 227. This image is dominated by a strong unresolved UV nucleus. The faint feature $\sim 1.2''$ north of the nucleus is the ghost mentioned in § 2.

3C 231, M 82

The UV image of 3C 231 is displayed in Figure 14 alongside the optical F555W image. Note that 3C 231 is not a powerful radio galaxies, but a famous starburst galaxy. The STIS $25''$ field of view represents a scale of 330 pc at distance of 3C 231. The STIS image thus only covers a small fraction of this large starburst galaxy. For reference, we include a larger scale F555W image (Figure 5). The entire STIS field of view is filled with UV emission showing spectacular bright and clumpy filamentary structures. There is also extensive diffuse emission, and compact clusters of star formation and individual point sources that may be individual O stars. There are a number of point source detected in the UV image that are not detected in the optical image.

3C 236

The UV image of 3C 236 is presented in Figure 15a. The knot at the center of the UV image shown here is identified with the nucleus of the galaxy. Three $\sim 0.3''$ scale bright knots of UV emission are visible along an arc which coincides with the SE edge of the dust lane visible in the optical image (Figure 15b). A fainter knot is also visible at the northern extreme of this arc $1.1''$ NE of the nucleus. The two brighter UV knots have counterparts in the optical image. Weak and diffuse UV emission is also detected between the knots. The properties of the UV knots in this source have been presented in O'Dea et al. (2001). They interpret the four knots (apart from the nucleus) in an arc along the edge of the dust lane as star forming regions, and discuss the possible relationships between the episodic outbursts of the very large radio source, and the young regions of star formation.

3C 270 (NGC 4261)

This galaxy contains a well defined disk of dust and gas which surrounds the unresolved nucleus. The structure and dynamics of this disk has been well studied by Jaffe et al. (1993, 1996); Ferrarese, Ford and Jaffe (1996). The UV image of 3C 270 (Figure 16) shows the disk clearly defined against the smooth background of the galaxy. The nucleus, prominent in the optical, is barely detected in the UV image. A faint cone, or jet of UV emission, with apex centred on the nucleus can be traced $0.5''$ from the nucleus to the eastern edge of the disk. The southern edge of this UV emission structure appears to be related to the dust filament that is apparent in the F547M image (Martel et al. 2000). The dust filament is also evident as UV extinction outside the SW edge of the disk.

The UV emitting cone may be the northern red feature shown in Martel et al. (2000), in which

case scattering from the dust of a bright nucleus would be implied. Alternatively, this east-west extension is along the radio jet and may be synchrotron in nature.

3C 285

Figure 17 shows the optical and UV images of 3C 285. This galaxy has a very chaotic morphology, with multiple large and small scale irregular dust lanes. There appears to be two main dust systems which are elongated perpendicular to one another. The smaller system, aligned roughly along PA 5 degrees, obscures the nucleus. The larger system aligned along PA 330 degrees intersects the smaller system at about 2″ distance from the nucleus, and defines a large ridge of extinction which crosses the entire PC chip (Figure 17b). The UV image reveals clumps of emission which are predominantly located along the edges of both the small and large scale dust lanes. These clumps are suggestive of star formation along the edges of dust lanes. Faint diffuse emission is also detected in the UV image, and the dust lanes are apparent in a smoothed version of the image.

3C 293

The UV image of this object (Figure 18a) reveals bright clumps embedded in filamentary diffuse emission. The large scale structures of the filaments are aligned along the same position angle as the dust lanes seen in the optical image (Figure 18b). Sub-structure within the filaments define strings of small sources in the shape of arcs and possibly one ring. There are also features that are reminiscent of bow shock morphology. Most of the UV features do not have optical counterparts. The only strong correlation with the optical image is for the small (1″) V-shaped feature which matches the extension of the optical emission approximately 1″ NE of the eastern nucleus. The UV emission does not show any relationship to the radio jet and the nuclear peaks are not detected in the UV.

3C 296

The UV image of this galaxy, Figure 19a, shows a well defined, smooth dust disk. The SE side of the dust disk is apparent in the UV image as extinction against the background galaxy emission.

3C 305

Figure 20a reveals extensive UV emission in 3C 305, with a diffuse fan of emission to the north of the nucleus. The extended UV emission consists of a complex of knots and filaments where the radio jet meets the dust disk to the East. This complex of UV emission also coincides with the major concentration of [O II] emission that lies just beyond the end of the radio jet (Jackson et al. 1995).

3C 310

The UV image of 3C 310, Figure 21a, displays an elongated central compact core of emission surrounded by very faint diffuse emission. The elongation is roughly aligned with the direction of the radio jet. The optical isophotes however are flattened in the direction of the radio jet (Figure 21b).

3C 317

The UV image of 3C 317 is presented in Figure 22a. It displays a relatively bright nucleus, and smooth host galaxy starlight. A very blue almost linear filament is evident in the UV image. The filament is ∼2 kpc in length and is located ∼4 kpc south of the nucleus. Martel et al. (2001) show the color of the filament is most consistent with a recent episode of star formation, but is not sufficient to represent the inferred amount of cooling gas if the cooling-flow model is correct. This source is an example of the presence of star formation which is *not* obviously correlated with the location of dust.

3C 321

The UV image of 3C 321 (Figure 23a) is spectacular. UV emission spans the entire region covered by the two galaxies seen in the optical image (Figure 23b) showing bright clumps, and V-shaped structures. The brightest UV emission occurs along the northern edge of the dust lane in the southern galaxy, and the brightest knot is coincident with the partially obscured nucleus. At least three bright knots can be discerned in this arc of emission that outlines the edge of the dust lane. UV emission blobs are detected curving up from the western end of the dust-lane towards the northern galaxy. From the UV image it is impossible to clearly demark the object into two separate galaxies. South of the dust there is a group of UV emission knots embedded in diffuse irregular ring feature. Some of the knots in this structure have corresponding features in the optical image, but others do not. (This feature is very suggestive of a 3-D cone with its axis pointing out from the nucleus of the galaxy.) In contrast to the relatively smooth and regular optical appearance of the northern galaxy, the UV emission corresponding to the northern galaxy is very irregular. The brightest region, centered on the northern galaxy (northern nucleus) is V-shaped with the apex directed toward the nucleus of the southern galaxy. Beyond the flare of the V-shaped feature, there is more diffuse filamentary UV emission which has no optical counterpart. At fainter levels the outline of the northern optical isophotes of the southern galaxy are apparent in the UV image.

The radio jet emanates from the nucleus of the southern galaxy, and follows the PA which remarkably passes through the northern neighbor. The spectroscopy of Robinson et al. (2000) shows that redshifts of these galaxies are equal to within 200 km s^{-1}, so these systems are definitely physically related.

3C 326

The UV image of 3C 326 presented in Figure 24a reveals a weak compact core, surrounded by faint diffuse emission against which the dust lane can be seen. The core shows some east-west elongation, which is most likely due to the dust lane, although this direction also roughly with the radio jet axis.

Note that there are two candidate galaxies for the identification of the optical counterpart to the radio source 3C 326. Both sources fall on the WFPC2 images, but only the southern counterpart was targeted by the STIS snaphot survey. Martel et al. (1999) also show the southern galaxy as

the radio source counterpart.

3C 338

The UV emission of 3C 338 is dominated by two bright point sources, (see Figure 25a). The brighter southern source coincides with the nucleus of the galaxy. We also detect very faint emission from the underlying galaxy starlight. The prominent optical dust feature (Figure 25b) can just be discerned in a smoothed version of the UV image. The northern point source has a faint optical counterpart.

3C 353

The UV and optical images of 3C 353 are presented in Figure 26. The heavily smoothed UV image shows a weak detection of UV emission. As noted in Martel et al. (1999) the optical image shows very round outer isophotes, with an inner elongated core which roughly aligns with the direction of the radio jet. The very faint smoothed UV emission also shows elongation in this direction, although this emission is only marginally above the noise.

3C 382

The UV image of 3C 382 (Figure 27a) is dominated by the strong nucleus. The faint object $1.5''$ NW of the nucleus is the ghost described in § 2

3C 388

Figure 28 displays the UV and optical images of 3C 388. The UV image shows a compact core plus a weaker UV source located $0.5''$ SW of the nucleus. This secondary source is aligned with the direction of the radio jet so we speculate that this feature may be a UV jet, or is in some way associated with the radio jet. The optical image (Figure 28b) also shows a weak source next to the compact core, but its position is $\sim 0.1''$ north of the UV jet candidate, and instead corresponds to an even weaker (highly uncertain) UV source at that location. None of the companion galaxies seen in the optical image, and described in Martel et al. (1999), are detected in the UV image.

3C 390.3

A bright UV nucleus dominates the UV image of 3C 390.3 (Figure 29a). The faint source south of the nucleus is the ghost image mentioned in section 2. We do not detect the underlying host galaxy starlight in this source.

3C 405 (Cygnus A)

The UV and optical images of 3C 405 are presented in Figure 30. The UV image displays complex and extended emission with resolved bright $\sim 0.3''$ scale clumps embedded in diffuse emission. This famous object has been the target of many HST imaging programs (Tadhunter et al. 2000, 1999; Jackson, Tadhunter & Sparks 1998). The F555W optical image is provided for reference in Figure 30b, and F336W, F450W, F662W images on the same scale are available in Jackson, Tadhunter & Sparks (1998). The F555W image, while dominated by [O III] line emission,

highlights most of the major morphological features seen in the optical images. The UV image presented here, most closely resembles the emission-line subtracted (ie. continuum) F336W image in Jackson, Tadhunter & Sparks (1998). Our UV image displays the blue compact features (labeled 1-8 in Figure 5 of their paper) with much higher contrast and signal to noise. The similarity of the UV image to these continuum images suggest that the UV emission is also dominated by continuum rather than line emission. Jackson, Tadhunter & Sparks (1998) identify the blue compact condensations as star formation regions, with the possible 10% contribution from nebular emission. They also find that the extended diffuse emission is most likely to be scattered radiation from an obscured quasar. The gap through which the radio jet passes is seen in the UV image. Note that observations of this target are subject to high galactic reddening of $E(B-V) = 0.381$ (see table 2) due to its low galactic latitude.

3C 449

The UV image of 3C 449 shown in Figure 31a reveals a well defined $\sim 3''$ scale disk structure, with significantly stronger UV emission in the northern half of the disk. The disk is made up of concentric elliptical arcs which have a similar size and clumpiness as the optical dust features seen in the dust lane in the optical image (Figure 31b). The position angle of the UV disk major axis is 168, which is approximately 13 degrees offset with respect to the optical dust disk axis. The western edge of the UV disk matches the curvature of the inside edge of the dust lane, and there is no UV emission within the dust lane regions. The UV emission does however resemble the ionized gas distribution as shown in Martel et al. (2000) with the brightest Hα emission in coincidence with the brightest UV emission.

3C 452

A heavily smoothed UV image of 3C 452 is shown in Figure 32a. No UV emission is detected in this image. Note that the lower throughput F25CN182 filter was used for this observation because of the bright star west of the field.

3C 465 (NGC 7720)

The UV image of 3C 465 is presented in Figure 33a. This image reveals a compact core of UV emission surrounded by faint diffuse emission which extends over a scale of approximately $5''$. The diffuse emission is clearly due to the galaxy starlight. The inner region shows a disk structure in absorption against the galaxy starlight . The morphology is similar to the dust disk seen in 3C 270, but the contrast between the dust disk and the background galaxy emission is less in the case of 3C 465. Also, 3C 465 shows a compact core which is not seen in 3C 270. The optical F702W image of 3C 465 is shown in Figure 33b. It displays a compact central core and an elongated ring of dust extinction. The dust ring has a projected diameter of $\sim 2''$, and width of $\sim 0.2''$. The outer edge of the optical dust ring corresponds to the radius of the dust extinction seen in the UV image (Martel et al. 2000).

3.3.   Summary of UV Morphologies and Scales

In this section we summarize the diverse range of UV morphologies and emission structures displayed in Figures 7 to 33. Some objects exhibit similar features which allows us to perform a rough categorization into six groups based on the morphology and scale of the UV emission. Figure 34 shows the categorized objects where each row of images comprises a single category. Figure 34 is arranged such that the first four rows display the groups with extended UV emission in order of increasing physical size.

3.3.1.   Dust Disks

The objects which display a dust-disk morphology (3C 40, 3C 270, 3C 296, 3C 449 and 3C 465) define a remarkably uniform category in terms of the scale and physical structure of the of the UV emitting region. These objects are shown in Figure 34 (top row) on the same physical scale (2.0 kpc box). The three most similar of these objects, 3C 40, 3C 270 and 3C 296, show UV emission that unambiguously comes from the smooth underlying elliptical host galaxy, with the dust disk apparent in absorption against the background UV galaxy light. The other two objects in this group, 3C 449 and 3C 465 clearly have similar scale disk structures, and include contribution from the host galaxy starlight, however we note that the detailed UV morphologies of these two dust disks differ from 3C 40, 3C 270, and 3C 296. In the case of 3C 449 the dust disk structure is seen both in emission and absorption. In 3C 465 the disk is not as regular as 3C 40, 3C 270, or 3C 296 and the source contains a compact central core. We also note that 3C 40 is the only object in this group with no compact core seen in the optical image.

3.3.2.   Dust Associated Star Formation

Another striking group of objects are those which exhibit bright extended UV emission over scales of 5 to 20 kpc. In a number of cases this large scale emission is clearly associated with the galaxy dust lane, and in all cases where this is true, the dust lane displays a very unsettled and chaotic morphology (3C 285, 3C 293, 3C 236 and 3C 321). In all these cases the UV emission appears to be star formation. This group of objects is displayed with a uniform box size of 20 kpc in the third row of Figure 34. We note that the UV morphology in these objects is comparable to the rest-frame UV structures seen in optical images of HZRG, and return to this result in the discussion section.

3.3.3. Complex Extended UV Emission

The objects 3C 405, 3C 305, 3C 192 and 3C 198 also display bright, extended and interesting UV morphology. The emission is typically extended over a 5 kpc scale in these objects. While these objects display quite similar features to the *dust associated star formation* group, we assign them to a separate group because the UV emission is not so clearly identified as star formation, and these objects may represent the presence other UV emission mechanisms. For example, in 3C 405 the bright UV clumps are most likely due to the young star forming regions (Jackson, Tadhunter & Sparks 1998), but the geometry and presence of strong optical emission lines leads us to expect some contribution from for ionized gas and scattered UV emission. The UV emission in 3C 305 is closely related to the dust lane and may be star formation, however the more diffuse distribution of the UV emission makes this uncertain, and scattered light from the jet may play a role. 3C 192 is smaller, but morphologically similar to 3C 305 and may also be dominated by scattered light. We loosely categorize these objects as *complex extended* UV emission. The UV images of the objects in this category are displayed in the fourth row of Figure 34 with a box size of 10 kpc.

3.3.4. Compact Core plus Galaxy or Jet Components

A number of objects show compact cores, in combination with a significant contribution from the underlying elliptical galaxy starlight (eg. 3C 310, 3C 35). Some of these objects also display extra UV emission features such as the prominent UV jet seen in 3C 66B, and the possible weak jet in 3C 388. Other objects with compact cores also exhibit absorption of the UV light by a relatively smooth dust lane as in 3C 326, or extra UV emitting sources such as the filament in 3C 317, and the additional UV point source in 3C 338. We group all these objects into a category called *compact core plus galaxy or jet components.* Clearly this is a less homogeneous group of objects, which represent a range of physical mechanisms. The UV images of these sources are displayed in the second row of Figure 34 with a uniform box size of 5.0 kpc.

3.3.5. Nuclear Dominated

Three of the objects in our sample 3C 227, 3C 382 and 3C 390.3, have very bright UV nuclei at their cores. All of these bright nuclei are all unresolved at the resolution of HST. The UV images of this *nuclear dominated* category are displayed in the fifth row of Figure 34 with a box size of 10 kpc.

3.3.6. UV Host Galaxy and Weak Detections

The remaining objects consist of the weakly detected UV emission in 3C 353, and the very faint nucleus plus galaxy host emission detected in 3C 29. We display this category in the last row of Figure 34 with a box size of 10 kpc.

4. ANALYSIS

In this section we make quantitative comparisons of the UV, optical and radio properties of all the objects in the sample. We investigate how these properties vary as a function of UV morphology, and compare the total integrated UV and optical luminosities to theoretical model predictions of (i) star formation and evolution, and (ii) ionized gas line emission. These comparisons are based on the extinction-corrected, total UV and optical integrated luminosities from Table 4, and the radio properties listed in Table 2. For this analysis we use the total integrated optical and UV luminosities, (rather than separating individual objects into separate components) since we intend for these results to be useful for luminosity and colour comparisons with higher redshift radio galaxies where only the integrated properties are accessible.

First we consider the UV and optical luminosities. Figure 35a shows the UV luminosity versus the F702W luminosity, and Figure 35b shows the UV luminosity versus F555W luminosity. All units are given as $\log_{10}(L/L_\odot)$, and selected individual objects are labeled with their 3C number. Note that 24 of the 27 sample objects were observed with the F702W filter, 17 were observed with the F555W filter, and 3 objects were observed only with the F555W filter, so there is an overlap of 14 objects which are plotted in both Figures 35a and 35b.

The most obvious feature in Figure 35 is the far higher dispersion in the UV luminosities as compared to the optical luminosities. While the optical luminosities range over one order of magnitude, the UV luminosities range over four orders of magnitude. Formally, the logarithmic dispersions (σ) are 0.30 and 0.29 for F702W and F555W[4] respectively and 0.93 for the UV luminosity.

This result is not surprising given the extraordinary range in morphology shown in Figures 7 to 33. Firstly, we expect a far higher dispersion in the UV than in the optical because of the wide range of UV emission processes indicated by the UV morphologies, compared to the optical where the emission in most cases is dominated by the old stellar population with varying amounts of dust extinction. Secondly, some of the processes which dominate the UV emission are intrinsically more likely to be subject to object-to-object variations. For example, star formation triggered by a merger event is a chaotic process, where the amount of star formation varies greatly with the

---

[4]3C 231 is excluded in calculation of F555W$_\sigma$ because it is a Starburst galaxy, and because the measurements only reflect a small region of the object. See Sections 2 and 3.2

details of the merger, (such as gas and dust content of merging systems, and impact parameter) and moreover the lifetime of the young hot UV-emitting stars is relatively short. The strength of scattered UV light is intrinsically variable from object-to-object because of the dependence on orientation, and geometry of the scattering medium. The presence of a bright UV nucleus in some objects also contributes significantly to the high UV dispersion of the total flux. Differential dust absorption will also contribute to the UV dispersion, but does not appear to be the dominant effect because of the clear presence of UV emission mechanisms.

Consider now the UV morphological classifications (described in section 3.3) that are indicated by different symbols in Figure 35. We find that the UV luminosity is indeed related to the morphological classifications. Firstly the three most UV luminous sources $(L/L_\odot > 10^9)$, 3C 382, 3C 390.3 and 3C 227 are all dominated by very bright point sources at their nuclei $(L/L_\odot > 10^9)$. The brightness of these sources is obviously due to the AGN out-shining the host galaxy in the UV by a factor of ~ 100 or more. 3C 321 also stands out as a very bright source, comparable in luminosity to the bright UV nuclei $(L/L_\odot = 1.58 \times 10^9)$, yet this source is does not show a strong nucleus, rather it is dominated by a bright arc of emission along the edge of this host galaxy's dust lane, with large scale extended filamentary and cone shaped diffuse emission. 3C 321 appears to be the extreme UV bright case of the objects classified in our morphological categories of *dust associated star formation* and of *complex extended*. All the objects in these two classes are bright in the UV, and there is a clear division at the UV luminosity of $L/L_\odot = 10^8$ between these sources, and the lower luminosity sources which fall into the other morphological classifications.

The groups of objects classified as *dust disks* and *compact core plus galaxy and jets* are intermixed in Figure 35, and have UV luminosities between 10^7 and 10^8 $L_\odot$. The dust disk objects appear to form a very coherent group with similar UV luminosities, sizes and morphological properties. As described in § 3.3, all of the dust disk objects clearly exhibit the same physical structure of a disk surrounding the central region of the galaxy. The possible differences in the UV emission processes within this group of objects (host galaxy old stellar population in 3C 40, 3C 270 and 3C 296, compared to scattering or ionization in 3C 449 and strong nuclear contribution in 3C 465) is not apparent in their UV or optical luminosities which show no systematic differences within the group.

The objects classified as *compact core plus galaxy and jets* are a less homogeneous group. The UV emission of these objects includes contributions from the non-thermal synchrotron jets, and the nuclei that are clearly identified in the images. These processes however, are not made apparent in the total integrated luminosities as displayed in Figure 35, where this group of objects show a similar range of luminosities as observed for the dust disk objects.

The least luminous sources in Figure 35 are those in which only the host galaxy starlight contributes to the UV flux. The very faint UV luminosity of 3C 353 is perhaps anomalous, or due to errors in the background subtraction of this weak source. The UV and optical luminosities of 3C 231 (M 82) plotted on Figure 35 represent the total luminosity of the $25''$ square region centred

on the nucleus of this starburst galaxy. The UV-optical colour of this region is similar to the fainter radio galaxy hosts described here.

In summary, comparison of the UV and optical luminosities as a function of their UV morphology described here shows that (i) the brightest UV sources are dominated by strong UV nuclear emission. (ii) Large scale UV emission features suggestive of star formation and scattering processes have luminosities well in excess of those galaxies dominated by old stellar populations, and in one case 3C 321 the luminosity is comparable to the nuclear dominated sources. (iii) Objects with compact cores and evidence for UV emission from jets, have total integrated UV luminosities that are similar to dust disk objects whose UV emission is dominated by the old stellar population of the host galaxy.

4.1. Physical Models: Star Formation and Ionized Gas

In order to obtain insight into the physical origin of the UV emission we compare the total integrated UV and optical luminosities to theoretical model predictions of (i) star formation and evolution, and (ii) ionized gas line emission. Here we describe the models that are to be plotted on the UV versus optical luminosity diagrams in section 4.2.

Star formation is clearly a major component of UV emission detected in our images. Using simplified models of the integrated emission we seek to identify and characterize the old stellar population of the host elliptical galaxy, and the populations of young UV-bright star forming regions found in our images. For this purpose we use a set of stellar population synthesis models from Bruzual and Charlot (1993) and, Charlot and Bruzual (2001), which have also recently been described in O'Dea et al. (2001) in relation to star forming regions in 3C 236. In general these models cover a variety of metallicity, IMF and both single burst and continuous star formation rates. Here, we use only the $0.004Z_{\odot}$ metallicity, Salpeter IMF models, and calculate the luminosities using the average redshift of the sample (0.0536). The model differences over the redshift range of the sample are insignificant for the model grids as presented here. Note that single burst models of ages 7 Gy and older provide colors expected for an underlying old stellar population.

In some cases the UV emission may come from ionized gas. An overlay of the STIS and WFPC2 filter bandpasses the spectrum of NGC 1068 Figure 6 shows the main UV lines concerned are C IV λ1550 and He IIλ1640 and C III] λ1909. As mentioned above, Lyman-α 1216Å falls within the UV bandpass for objects with z> 0.05, however due to the broad nature of the UV filter, the total flux is still dominated by the continuum emission (assuming a model shock spectrum, or the NGC 1068 spectrum).

The ionized gas models used here are shock models computed with the Mappings III plasma modeling code. Mappings III is an updated version of the Mappings II code described by Dopita & Sutherland (1995). Models of shock ionized gas were computed for shock velocities of $200 - 1000$ km s^{-1} with pre-shock density of 1 cm^{-3} and an equipartition magnetic field giving a magnetic

parameter of $B/\sqrt{n} = 3.22$ μG cm$^{3/2}$. For all the Mappings III models, the UV and optical fluxes were calculated by passing the model spectra into synphot, and extracting the fluxes using the appropriate bandpasses. The fluxes were then converted to units of L/L$_\odot$ using the average redshift of the sample.

In addition to star forming regions, and ionized gas, other UV emission processes will also contribute, or may even dominate the UV flux. In at least one case, 3C 66B, the UV emission is clearly due to non-thermal synchrotron radiation. Scattered UV emission may also an important component of the UV emission for the cases of 3C 321, 3C 305, 3C 449. These processes will be briefly discussed below (section 4.2), and detailed models for non-thermal-synchrotron, and scattered emission are deferred to future studies of the individual objects.

4.2. Comparison with models

In this section we compare the UV and optical luminosities to the star formation and ionized gas emission models described above. For each set of models we plot the model grid, and the data on diagrams of UV luminosity versus F702W luminosity, and of UV luminosity versus F555W luminosity, where all luminosities are given in units of $\log_{10}(L/L_\odot)$.

Figures 36 and 37 show overlays of star formation models calculated for the average redshift of the sample. The first set of diagrams displayed in Figure 36 show the models for the case of a *constant star formation rate*. As described above, the constant star formation models consider the luminosity evolution of a stellar population in which star formation occurs continuously,

The model tracks shown with solid lines in Figure 36 trace the UV and optical luminosities as a function of the age of the stellar population. The ages are indicated on the tracks, in units of $\log_{10}(years)$, up to a maximum age of 2×10^{10} years. The continuous, constant star formation rate used in these models, causes the total luminosity and mass of the modeled population to increase with age, hence the tracks evolve toward the upper right corner of the diagrams in Figure 36. The various tracks shown, and connected by dashed lines of constant age, represent different total masses of the evolved 10^{10} year old populations. The total masses of the models shown are 10^{13} to 10^8 M$_\odot$. These various tracks were simply derived from a single *constant star formation rate* model, by scaling the total mass. Since the luminosity scales linearly with the mass of the model, the dashed lines all have a gradient of 1.0. While this scenario may be unphysical due to the fueling requirements (input of gas and dust from which stars form) to maintain a constant star formation rate over these timescales, we nevertheless include the tracks here to represent one extremum of star formation.

The majority of the data cannot be described by such models. The four objects which do fall within the grid are also excluded because they are strongly dominated by luminous nuclei. We conclude that constant star formation models are not applicable.

Figure 37 shows model tracks for *single burst star formation*. These models consider the luminosity evolution of a fixed mass of stars, in which all the stars are born at the same time. The models predict that the UV and optical luminosity of such a population stays relatively constant over the first 10^6 years, then slowly fades. Over a typical 10^{10} year lifetime, the UV luminosity decreases by 4 orders of magnitude, while the optical luminosity decreases by approximately 1.5 orders of magnitude. Hence the model tracks shown in Figure 37 evolve in the opposite sense to the previous constant star formation models, and decrease in luminosity as a function of age. Again the maximum age considered is 2×10^{10} years, and the various tracks shown represent initial population total masses of 10^{11} to 10^7 $M_\odot$. Note that the total mass of the population remains constant with age in the single burst scenario, and no attempt is made to include mass loss. The strong UV evolution shown by these tracks make the UV luminosity a sensitive function of the age of the population, and can in principle provide an important discriminant for the old versus young populations of stars that contribute to the UV appearance of the galaxies in our sample.

A significant number of the objects could indeed be described by such a single burst model. All the dust-disk objects are concentrated in the diagram around the region predicted for an old ($\sim 10^{10}$ years) evolved stellar population of 10^{10} to 10^{11} $M_\odot$. This is consistent with these sources being dominated by the host elliptical galaxy star light, with a small correction for dust extinction.

Comparing Figure 37a and 37b for consistency between inferred model parameters using the UV-F702W colours and the UV-F555W colours we find that the UV bright UV objects common to both the F702W and F555W diagrams (3C 198, 3C 236, 3C 285 and 3C 305) fall relatively close to the same location in each diagram with respect to the model parameters. The difference is a uniform small shift in the sense that the models shown in Figure 37b indicate a slightly younger, less massive population. This effect however could also be mimicked by reddening.

Excluding the nuclear dominated sources we find that all the UV bright sources (categorized as *dust associated star formation* and *complex extended*) fall within the single burst star formation models. This confirms that the colours of those sources, like 3C 285, 3C 236 and 3C 293 where the morphology suggests that star formation is the dominant UV process, can be explained by stellar emission. Clearly these sources are not a single population, rather mixtures of old and young single burst populations.

To explore this idea in more detail we calculated a mixing model which includes varying contributions from young and old populations of stars. In this simplified case we use luminosities of the old and young extremes of the single-burst population models described above as the mixing components. Figure 38 shows the mixing model tracks for the same total masses as were considered above for the single burst models. The tick marks along the tracks represent the luminosity fractions of young to old components. The mixing lines show that a small amount of young star formation has a significant effect on the UV luminosity. A number of the objects are clearly consistent with such a scenario based on the presence of star forming morphology, and the match of the integrated colours expected for such a mixed population.

Figure 39 illustrates the UV and optical luminosities predicted by Mappings III models of shock ionized gas. The solid lines of the model grid represent the luminosities for shock velocities varying from 100 to 1000 km s^{-1}, with a constant physical shock-front area. Both the UV and optical luminosities of shock excited gas are strong functions of the shock velocity, increasing by 3 orders of magnitude over the velocity range considered here. The various shock model tracks shown in Figure 39 have been scaled by the shock front area in multiples of 10. The resulting model grid spans only a narrow region of the parameter space on Figure 39, and due to the similar luminosity scaling with shock velocity and shock-front area the grid is highly redundant. Nevertheless Figure 39 shows that shock excited gas may generate broadband UV and optical luminosities in the observed range. The majority of the data points do not fall within the shock model grid. Those objects that do, 3C 321, 3C 198, may indeed have contribution from emission lines. We also note that there is no systematic difference between the objects in our sample which contain Lyman Alpha in the bandpass, and those which do not suggesting that emission lines are not dominant.

Figures 40 shows the UV luminosities plotted against their total radio power at 178 MHz. In Figures 40a the UV classifications are indicated. There is no correlation on this diagram between the large scale, low frequency radio power and UV luminosity. On the other hand, if we distinguish the objects by their radio morphological types, FR-I, and FR-II (Fanaroff & Riley 1974) then we see that the two classes are distributed differently on the diagram (Figure 40b). The FR-I low power sources all have roughly the same UV luminosity, whereas the FR-II high power sources span the full range in UV luminosities observed in the sample. The FR-I sources include all the objects with dust-disk UV morphologies (except 3C 40 which is an FR-II). 3C 29, 3C 338 and 3C 66B are also FR-I sources. The FR-II sources include the larger scale dynamic and chaotic UV structures. Clearly the more dynamic UV emission processes occur preferentially in the FR-II sources, consistent with the idea that FR-II sources are associated with more disturbed host galaxy environment consistent with different fuelling of the AGN in FR-I and FR-II objects (Baum, Zirbel, & O'Dea 1995).

4.3.   Properties of the UV Nuclei

UV nuclei are clearly an important component of the UV emission of radio galaxies. Here we draw some broad conclusions about the nature of the nuclei observed in this sample. We defer the photometry and detailed analysis of the optical-UV properties of all the nuclei to Chiaberge et al. (2001). However, we can compare the integrated luminosities (νL_ν) of the three nuclear dominated galaxies (all of them being BLRG) with those of radio-loud QSO in the Elvis et al. (1994) sample. Limiting ourselves to the eight sources with z<0.3 from their sample, their median luminosity is $\sim 4 \times 10^{44}$ ergs s^{-1}, i.e ~ 1 order of magnitude more luminous than the average of our 3 nuclear dominated galaxies. Although this is consistent with the current unification scenario, in which BLRG are believed to be the less luminous counterparts of QSO, without any further spectral information we cannot establish whether they are intrinsically fainter or moderately

absorbed sources (observed through the edge of a nuclear obscuring torus, Dennett-Thorpe et al. 2000).

Most of the sources with optical compact cores also show compact cores in the UV. There are two objects (3C 270 and 3C 296) for which a UV counterpart is not found for the optical compact core. This may be due to either a steep nuclear spectrum, or extinction in the nuclear region. We note that in both these cases dusty extended structures are present.

Our observations show that the nuclei of radio galaxies are indeed bright in the UV and are in most cases visible with greater contrast against the background galaxy than in the optical images. However we do not find any UV compact cores in the sources that do not have optical compact cores. This suggests that if they are intrinsically present in these galaxies, as expected in the frame of the unified model, they are obscured in both the optical and in the UV by either nuclear or extended scale structures.

4.4.   Jets

A strong one-sided UV jet is detected in 3C 66B. 3C 270 and 3C 388 have possible weak UV jets, and the nuclei of 3C 192, 3C 310 and 3C 326 show elongation in the direction of their radio jets. In order to observe UV emission from synchrotron processes, electron energies must be high (with corresponding very brief lifetimes), and in situ acceleration must be required. Relativistic beaming effects may play an important role, both in boosting the intensity of radiation and also in blue-shifting the synchrotron break frequency which elevates the UV emission. There may be other examples of synchrotron radiation amongst the features we observe, however additional observations and detailed comparisons with radio structures would be needed, and are beyond the scope of this paper.

4.5.   Scattering

We identify 3C 270, 3C 321, 3C 305, 3C 405, and 3C 449 as candidates for scattered UV emission based on their morphology. Both 3C 321 and 3C 405 show conical structures which are likely the result of illumination by a strong hidden nuclear source.

In 3C 305 and 3C 192 the radio jet is roughly aligned with the extension of the UV emission, suggesting that in these cases we may be observing scattered jet photons.

Two of the dust disk like objects, 3C 270 and 3C 449 show signs of scattered emission. In 3C 270, the UV enhancement at the western edge of the disk may represent scattered nuclear continuum, or possibly scattered jet photons. These two sources are however both FR 1 type objects which according to some authors, are not expected to have a a strong (hidden) source of UV continuum available to be scattered. Baum, Zirbel, & O'Dea (1995) find that emission-line gas

in FR 2 objects are photoionized by strong nuclear UV continuum, and that FR 1 objects are not. This apparent lack of a strong ionizing UV continuum source in FR 1 objects, suggests that we may not expect to find significant levels of scattered UV nuclear light in the FR 1 objects in our sample.

5. Discussion

As described in the above classifications of our UV images, we find that the processes of star formation, nuclear emission, scattering, and extinction by dust, are the basic components which determine the UV appearance of low redshift radio galaxies. The relationships between these various components provide clues to the physics, merger history and evolution of radio galaxies. These same processes are also the likely ingredients which determine the appearance of HZRG.

We defer detailed analysis of the multiwavelength properties and of the individual objects to future papers. Here we briefly discuss some implications of the star forming regions found in the 3C radio galaxies, and make a broad comparison of the low redshift UV morphologies with high redshift radio galaxies.

We find a progression of UV morphologies from highly chaotic dusty systems with strong star formation, to smooth regular systems with nuclear dust-disks that are aligned perpendicularly to the radio jet. This range of morphologies appeals to a scenario where the central regions of radio galaxy hosts may evolve from highly chaotic systems, to more stable regular systems. This idea is linked with the merger scenario for the triggering and fueling of the active nucleus. In this evolutionary scenario the categories of objects identified in this paper may roughly represent the various stages of the effect of infalling gas and dust. For example the large scale chaotic dust lanes of the *dust associated star formation* group may represent the earliest stages of a merger event. The radio axes of these objects bear no relation to the dust lanes or central structures in these galaxies, perhaps indicating that these systems have not had enough time to settle into a stable configuration. At the other extreme the *dust disk* objects do not show strong evidence for star formation associated with the dust, and these regular dust disks may represent the final stable configuration. In all the dust disks the radio jet is aligned roughly perpendicularly to the major axis of the disk.

One of the difficulties with such a simplified scenario is that the timescales for settling of gas is of order 1 Gy after the merger (Gunn 1979; Christodoulou & Tohline 1993), which is longer than the $\sim 10^7$ year duration of a single epoch of radio activity (Alexander & Leahy 1987). If a merger resulted in only a single epoch of radio activity, then there would not be enough time for evolution from a 3C 293 like object into a settled dust disk within the lifetime of the radio jets. The evolutionary scenario may however be credible if the onset of radio activity occured (or re-occurred) at a time after the merger, perhaps dependent on the precise parameters of the encounter. These parameters may include merger impact geometry and gas infall timescale, also

the gas and dust content of the merging systems, and the angular momentum loss rate. If the onset of radio activity occurs at random time during a merger we may be able to account for the coexistence of radio jets and the wide range of morphologies as described here. Alternatively FR-I sources may be intriniscally different due to a different low accretion fuelling rate for the AGN as described in Baum, Zirbel, & O'Dea (1995).

Estimating the ages of the newly triggered star formation may provide a means of dating major merger events in the history of the host galaxy. Similarly, if star formation is related to the nuclear activity of the galaxy, the star formation ages will significantly aid our understanding of these systems as has recently been demonstrated by O'Dea et al. (2001) for the case of 3C 236 (using the UV and optical data described in this paper). They showed that the young star forming regions may be related to the inner 2 kpc scale radio source, and that the star formation may reflect the radio source history. Clearly many of the *dust associated star formation* objects show similarities to 3C 236 and we expect that more accurate dating of the individual star forming knots will shed light on the merger and activity history of these galaxies.

A primary motivation for UV imaging of low redshift radio galaxies is to provide a zero redshift comparison sample for the extraordinary rest frame UV morphologies found at high redshift. High resolution HST images of high redshift radio galaxies have been described by Best, Longair and Röttgering (1997) (28 3CR radio galaxies $0.6 < z < 1.8$) and Pentericci et al. (1999) (9 distant radio galaxies $2.3 < z < 3.6$). In both of these samples the optical observations sampled the rest frame UV of the radio galaxies, providing an ideal comparison for the rest frame UV emission of low redshift galaxies presented here. In general these objects display a spectacular range of structures, some but not all are aligned with the radio structures. The morphology of the emission varies greatly from a single bright patch to strings of knots stretching along the radio source. The UV emission of most objects is clumpy and irregular, consisting of a bright nucleus and fainter components. Some of the structures may be due to distributed dust.

A common feature in high redshift radio galaxies is that the optical and radio structure align, implying a fundamental relationship between the jets, and the host galaxy. Best, Longair, & Rottgering (1996); Best, Longair and Röttgering (1997) and Pentericci et al. (1999) find that the UV continuum is generally elongated along the radio source axis, although the characteristics of the alignment differ from case to case suggesting that the alignment is not the result of a single physical mechanism.

In general the low redshift radio galaxies do not show the high degree of alignment as observed at high redshift. Within the 27 objects presented in this paper we find only 2 objects show rough alignment of their UV emission with the direction of the radio jet with some similar characteristics to that seen at high redshift. The extended UV emission observed in 3C 321 is the most obvious case. The conical features are similar to that seen in the high redshift radio galaxy TX 0828+193 (Pentericci et al. 1999). We note however that 3C 321 is highly complex with strong star formation along the dust lane which is in general not observed in the high redshift sources. 3C 305 also

displays elongation of the UV emission along the direction of the radio jet. 3C 305 is similar to MRC 0943-242(Pentericci et al. 1999) in terms of UV emission morphology, and radio source size. 3C 405 is unique in the sample being by far the most powerful radio galaxy, with total luminosity similar to $z \sim 1$ radio galaxies. The UV emission in 3C 405 is clearly related to the axis of the radio jet in that the UV emission is distributed in the bi-conical structure obvious in emission-line images of this galaxy. The UV emission consisting of star forming regions and possible scattered light is however not elongated in the direction of the radio jet.

The UV images of low redshift ($z < 0.1$) radio galaxies presented here provide a high quality database for studying many important issues for our understanding of radio galaxies, and galaxy evolution in general. Using integrated properties we have shown that it is possible to characterize the star forming regions around the edges of the chaotic dust lanes seen in some of these objects. This has implications for dating the important events in the histories of these systems. Detailed studies of the individual objects are expected to provide insight into the relative roles of gas, dust, jets and star formation in radio galaxy hosts. In addition these data provide important constraints for identifying and characterizing the processes of scattering and ionization, and the spectral energy distributions of the radio galaxy nuclei and jets.

REFERENCES

Alexander, P. & Leahy, J. P. 1987, MNRAS, 225, 1

Allen, M. G., Dopita, M. A., Tsvetanov, Z. I. 1998, ApJ, 493, 571

Baum, S. A., Heckman, T. M. 1989, ApJ, 336, 702

Baum, S. A., Zirbel, E. L., & O'Dea, C. P. 1995, ApJ, 451, 88

Bennett, A. S., 1962a, MNRAS, 68, 163

Bennett, A. S., 1962b, MNRAS, 125, 75

Best, P. N., Longair, M. S., Röttgering, H. J. A. 1997, MNRAS, 292, 758

Best, P. N., Röttgering, H. J. A., Longair, M. S. 2000, MNRAS, 311, 23

Best, P. N., Longair, M. S., & Rottgering, H. J. A. 1996, MNRAS, 280, L9

Bicknell, G. V., Sutherland, R. S., van Breugel, W. J. M., Dopita, M. A., Dey, A., & Miley, G. K. 2000, ApJ, 540, 678

Blundell, K. M., Rawlings, S. 1999, Nature, 399, 330

Brown, T. M., 1996, thesis, Johns Hopkins University, USA

Brüggen, M. & Kaiser, C. R. 2001, MNRAS, 325, 676

Bruzual, A.G., & Charlot, S., 1993, ApJ, 405, 538.

Cardelli, J. A., Clayton, G. C., & Mathis, J. S. 1989, ApJ, 345, 245

Capetti, A., Macchetto, F., Sparks, W. B., Miley, G. K. 1994, å, 289, 61

Chambers, K., Miley, G. K., van Breugel, W. 1987, Nature 329, 604

Charlot, S., & Bruzual, A.G., 2001 in preparation.

Chiaberge, M. (in preparation)

Christodoulou, D. M. & Tohline, J. E. 1993, ApJ, 403, 110

de Koff, S., Baum, S. A., Sparks, W. B., Biretta, J. Golombek, D., Macchetto, F. D., McCarthy, P., Miley, G. K. 1996, ApJS, 107, 621

Dey, A., van Breugel, W., Vacca, W. D., & Antonucci, R. 1997, ApJ, 490, 698

Dopita, M. A., & Sutherland, R. S. 1995, ApJ, 455, 468

Elvis, M. et al. 1994, ApJS, 95, 1

Fanaroff, B. L. & Riley, J. M. 1974, MNRAS, 167, 31P

Ferrarese, L., Ford, H. C., Jaffe, W. 1996, ApJ, 470, 444

Ferrarese, L. & Merritt, D. 2000, ApJ, 539, L9

Gunn, J. E. 1979, Active galactic nuclei. (A79-50785 22-90) Cambridge, Cambridge University Press, 1979, p. 213-225.

Hardcastle, M. J., Birkinshaw, M., & Worrall, D. M. 2001, MNRAS, 323, L17

Hill, G. J. & Lilly, S. J. 1991, ApJ, 367, 1

Jackson, N., Sparks, W. B., Miley, G. K., Macchetto, F. D. 1995, A&A, 296, 339

Jackson, N., Tadhunter, C., Sparks, W.B., 1998, MNRAS, 301, 131

Jaffe, W. Ford, H. C., Ferrarese, L., van den Bosch, F., O'Connell, R. W., 1993, Nature, 364, 213

Jaffe, W. Ford, H. C., Ferrarese, L., van den Bosch, F., O'Connell, R. W., 1996, ApJ, 460, 214

Lehnert, M. D., van Breugel, W. J. M., Heckman, T. M., Miley, G. K. 1999b, ApJS, 124, 11

Lehnert, M. D., Miley, G. K., Sparks, W. B., Baum, S. A., Biretta, J. Golombek, D., de Koff, S., Macchetto, F. D., McCarthy, P. J. 1999 ApJS, 123, 351

Magorrian, J., Tremaine, S., Richstone, D., Bender, R., Bower, G., Dressler, A., Faber, S. M., Gebhardt. K., Green, R., Grillmair, C., Kormendy, J., Lauer, T. 1998, AJ, 115, 2285

Martel, A. R., Sparks, W. B., Macchetto, D., Biretta, J., Baum, S. A., Golombek, D., McCarthy, P. J., De Koff, S., Miley, G. K. 1998, ApJ, 496, 203

Martel, A. R., Baum, S. A., Sparks, W. B., Wyckoff, E., Biretta, J. A., Golombek, D., Macchetto, D., De Koff, S., McCarthy, P. J., Miley, G. K. 1999, ApJS, 122, 81

Martel, A. R., Turner, N. J., Sparks, W. B., Baum, S. A. 2000, ApJS, 130, 267

Martel, A. R., Sparks, W. B., Koekemoer, A. M., Allen, M. G., Baum, S. A., Macchetto, F., 2001, AJ, submitted.

Matthews, T., Morgan, W., Schmidt, M. 1964, ApJ, 140, 35

McCarthy, P., van Breugel, W., Spinrad, H. et al 1987, ApJ, 321, L29

McCarthy, P., Miley, G. K., De Koff, S., Baum, S. A., Sparks, W. B., Golombek, D., Biretta, J., Macchetto, D. 1997, ApJS, 112, 415

O'Dea, C. P., Koekemoer, A. M., Baum, S. A., Sparks, W. B., Martel, A. R., Allen, M. G., Macchetto, F. D., Miley, G. K. 2001, AJ, 121, 1915

Ohl, R. G., O'Connel, R. W., Bohlin, R. C., Collins, N. R., Dorman, B., Fanelli, M. N. Neff, S. G., Roberts, M. S., Smith, A. M., Stecher, T. P. 1998, ApJ, 505, 11

Pentericci, L., Röttgering, H. J. A., Miley, G. K., McCarthy, P., Spinrad, H., van Breugel, W. J. M., Macchetto, F. 1999 A&A, 341, 329

Robinson, T., Tadhunter, C. N., Axon, D. J., Robinson, A. 2000, MNRAS, 317, 922

Schlegel, D. J., Finkbeiner, D. P., & Davis, M. 1998, ApJ, 500, 525

Smith, D. A., Wilson, A. S., Arnaud, K. A., Terashima, Y., Young, A. J., & Shopbell, P. L. 2001, American Astronomical Society Meeting, 198, 1702

Sparks, W. B., Baum, S. A., Biretta, J., Macchetto, F. D., 2000, ApJ, 542, 667

Sparks, W. B. in preparation

Spinrad, H., Djorgovsky, S., Marr, J., Aguilar, L. 1985, PASP, 97, 932

Tadhunter, C. N.; Sparks, W., Axon, D. J., Bergeron, L., Jackson, N. J., Packham, C., Hough, J. H., Robinson, A., Young, S., 2000, MNRAS, 313, 52

Tadhunter, C. N., Packham, C., Axon, D. J. Jackson, N. J., Hough, J. H., Robinson, A., Young, S., Sparks, W. 1999, ApJ, 512, 91

Yates, M. G., Miller, L., & Peacock, J. A. 1989, MNRAS, 240, 129

Zirbel, E. L., Baum, S. A., 1998, ApJS, 114, 177

Zirbel, E. L. 1996, ApJ, 473, 713

Fig. 1.— Full field of the STIS NUV MAMA observation of 3C 236, smoothed with a $\sigma = 21$ Gaussian kernel. Note the enhanced background around the edges of the frame, which is due to residuals from the dark current subtraction. The inner contour represents the source region, defined as 0.1 counts above the background. The background was measured in the region between the source and the 800 pixel diameter circle shown. The outer circle was adapted in cases where a possible source fell near its edge as in 3C 236 as shown.

Fig. 2.— Registered NUV MAMA and WFPC F702W frames. This example of 3C 236 shows the UV and optical images which have been *drizzled* onto the same pixel grid (STIS pixel size) including a N-E rotation and object registration. The object masks shown have also been appropriately rotated and registered in order to extract total fluxes from the same regions in the UV and optical images.
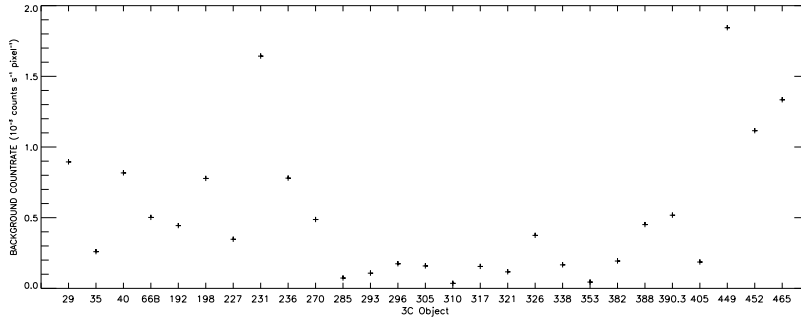

Fig. 3.— UV Background rate measurements. The UV background rates measured from the region outside the object region and inside the 800 pixel diameter circle, are shown for each object.
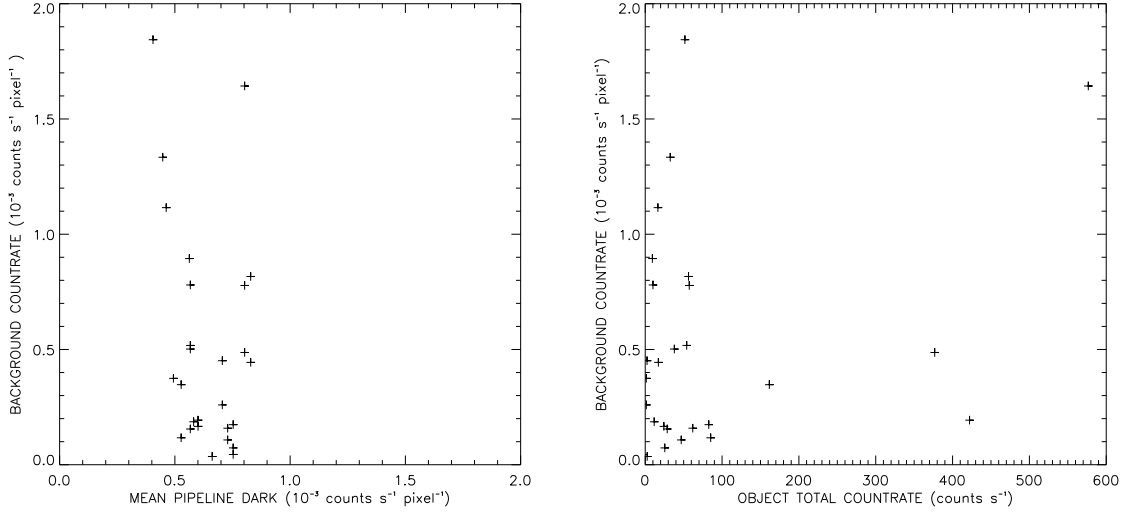
Fig. 4.— Background, Mean Dark and Total Object Countrates. (a.) The background countrate measured from our images is shown versus the mean dark countrate that was subtracted in the pipeline reduction of the images. Note that there is no correlation between these two countrates. (b.) The background countrate measured from our images is shown versus the total object countrate. There is no correlation of the object countrate rate with the background with the exception of 3C 231 (M 82) where the background is clearly overestimated due to emission covering the entire field of view. The lack of a correlation for the majority of the objects provides confidence in our background and total flux measurements
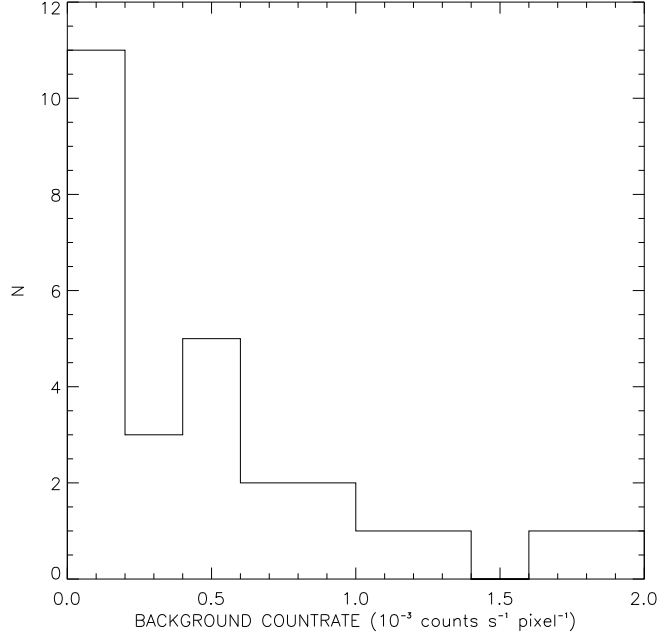
Fig. 5.— Histogram of the UV Background Rates. The background measurements as described in Section 2 are expected to be dominated by the sky background. With the observational parameters used the expected sky countrate is 6.25×10^{-6} to 1.2×10^{-3} counts s^{-1} pixel^{-1}. All but three of the objects fall within this range.
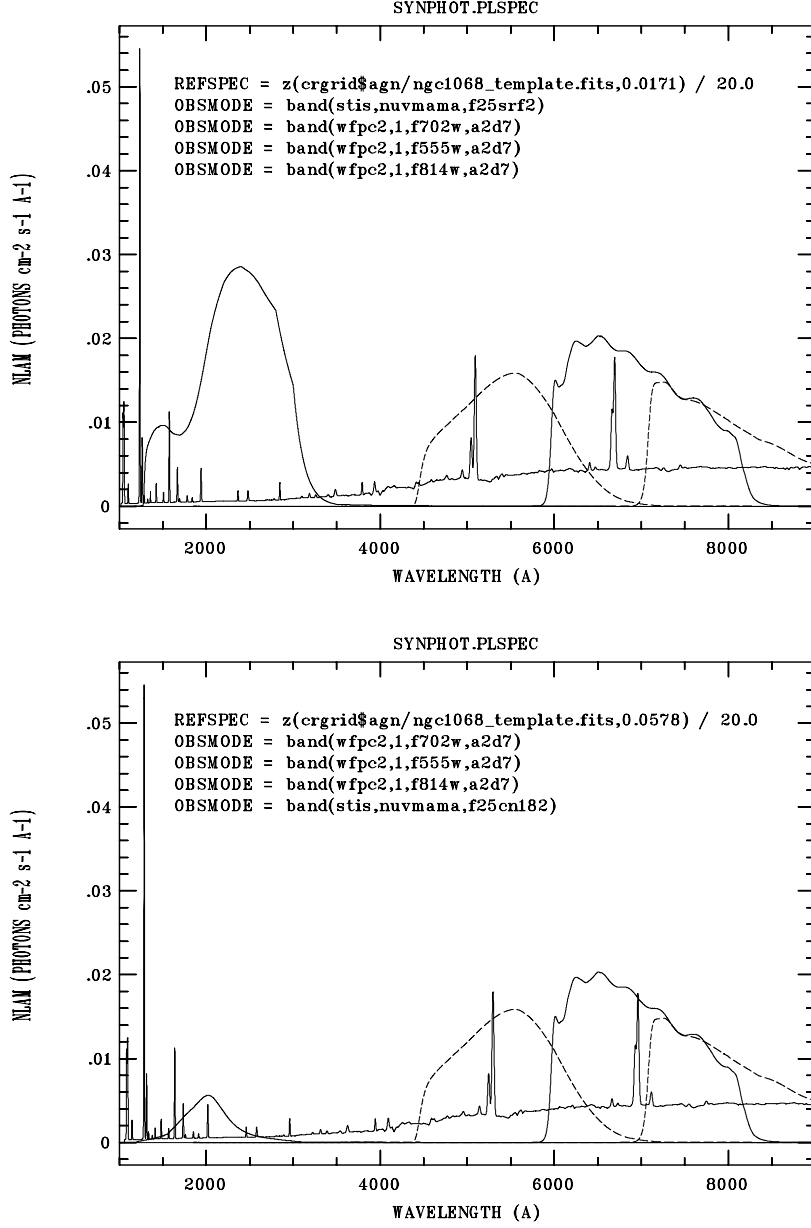
Fig. 6.— Band-passes of the HST STIS and WFPC2 filters. The STIS F25SRF2 and FCN182NM, and the WFPC2 F555W and F702W filter bandpasses are shown. For reference these bandpasses are overlaid on a spectrum of NGC 1068.

Fig. 7.— 3C 29: (a) STIS NUV MAMA image of 3C 29. The bar in the upper right corner of the image indicates the direction of the radio jet (Martel et al. 1999). A scale bar in kpc at the distance of 3C 29 is included in the lower right corner. (b) WFPC2 image of 3C 29.

Fig. 8.— 3C 35: Same as for Figure 7 but for 3C 35

Fig. 9.— 3C 40: Same as for Figure 7 but for 3C 40

Fig. 10.— 3C 66B: Same as for Figure 7 but for 3C 66B

Fig. 11.— 3C 192: Same as for Figure 7 but for 3C 192

Fig. 12.— 3C 198: Same as for Figure 7 but for 3C 198

Fig. 13.— 3C 227: Same as for Figure 7 but for 3C 227

Fig. 14.— 3C 231: Same as for Figure 7 but for 3C 231. Note that 3C 231 is not a radio galaxy so no radio axis direction is indicated.

rightmost WF chip.

Fig. 15.— 3C 236: Same as for Figure 7 but for 3C 236

Fig. 16.— 3C 270: Same as for Figure 7 but for 3C 270

Fig. 17.— 3C 285: Same as for Figure 7 but for 3C 285

Fig. 18.— 3C 293: Same as for Figure 7 but for 3C 293

Fig. 19.— 3C 296: Same as for Figure 7 but for 3C 296

Fig. 20.— 3C 305: Same as for Figure 7 but for 3C 305

Fig. 21.— 3C 310: Same as for Figure 7 but for 3C 310

Fig. 22.— 3C 317: Same as for Figure 7 but for 3C 317

Fig. 23.— 3C 321: Same as for Figure 7 but for 3C 321

Fig. 24.— 3C 326: Same as for Figure 7 but for 3C 326

Fig. 25.— 3C 338: Same as for Figure 7 but for 3C 338

Fig. 26.— 3C 353: Same as for Figure 7 but for 3C 353

Fig. 27.— 3C 382: Same as for Figure 7 but for 3C 382

Fig. 28.— 3C 388: Same as for Figure 7 but for 3C 388

Fig. 29.— 3C 390.3: Same as for Figure 7 but for 3C 390.3

Fig. 30.— 3C 405: Same as for Figure 7 but for 3C 405

Fig. 31.— 3C 449: Same as for Figure 7 but for 3C 449

Fig. 32.— 3C 452: Same as for Figure 7 but for 3C 452

Fig. 33.— 3C 465: Same as for Figure 7 but for 3C 465

Fig. 34.— 3C Radio Galaxies Categorized by UV Morphology and Scale. This figure presents all of the UV images of 3C Radio galaxies described in this paper. The images have been grouped into six categories based on their UV morphology and scale. Each category is displayed along a single row in this figure, and the physical box size of the image is constant are displayed here

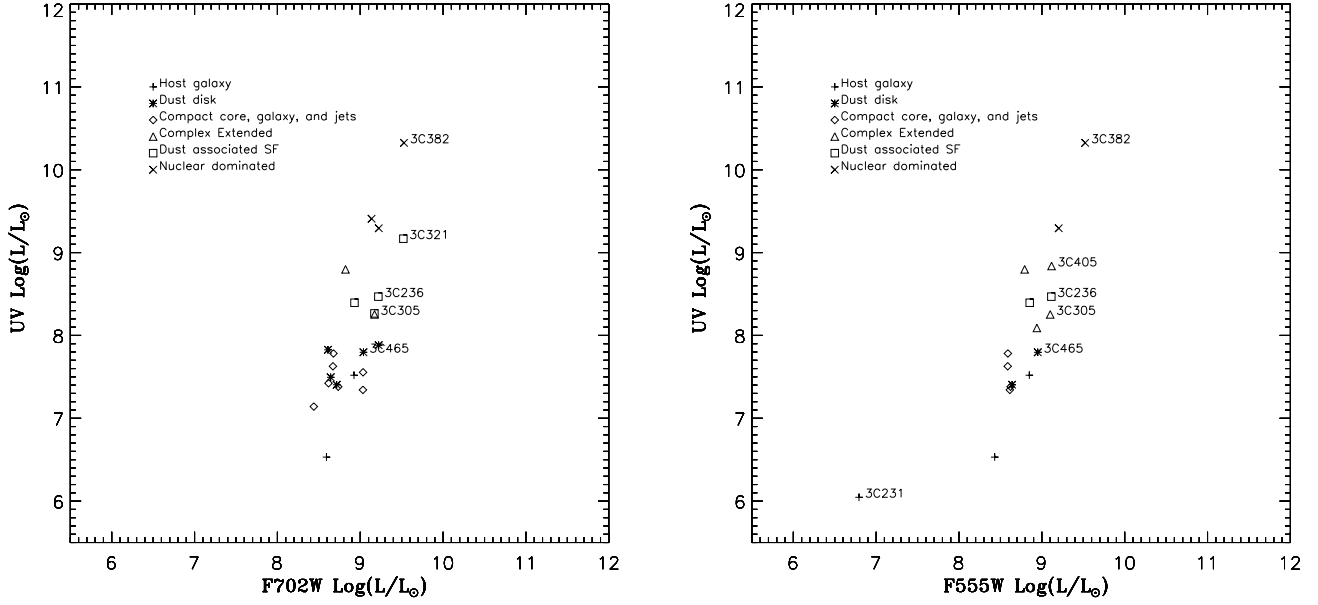Fig. 35.— (a) UV luminosity versus Optical F702W luminosity. (b) UV luminosity versus Optical F555W luminosity. The plotted point styles indicate the morphological classifications described in section 3.3
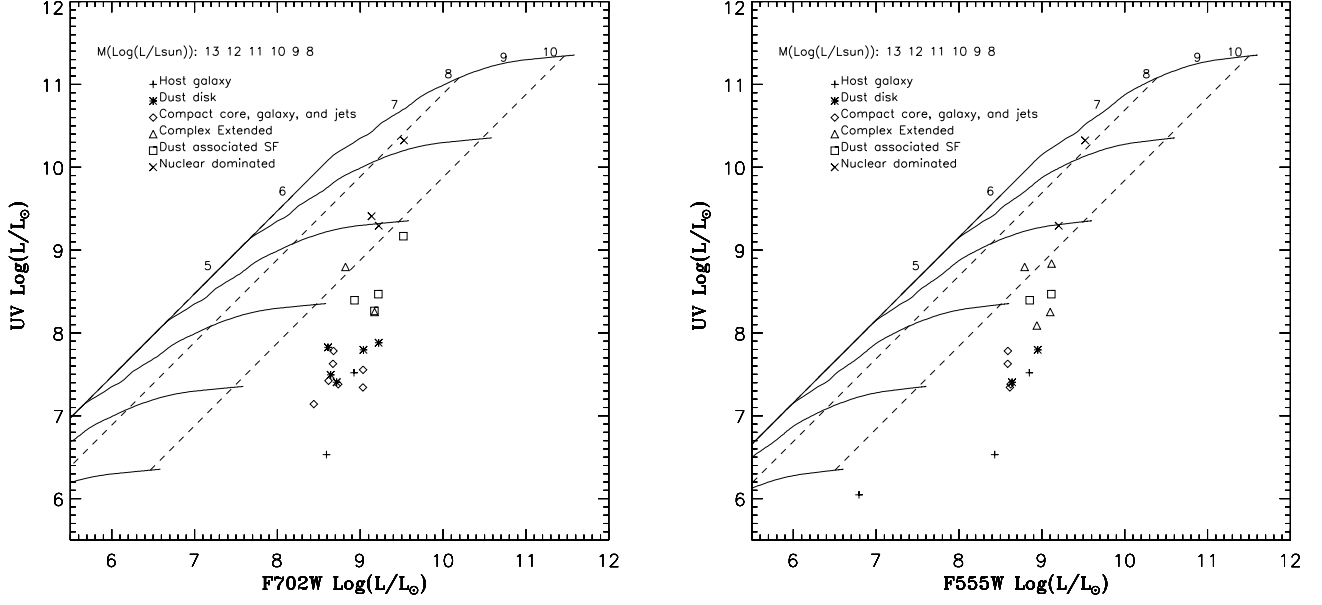
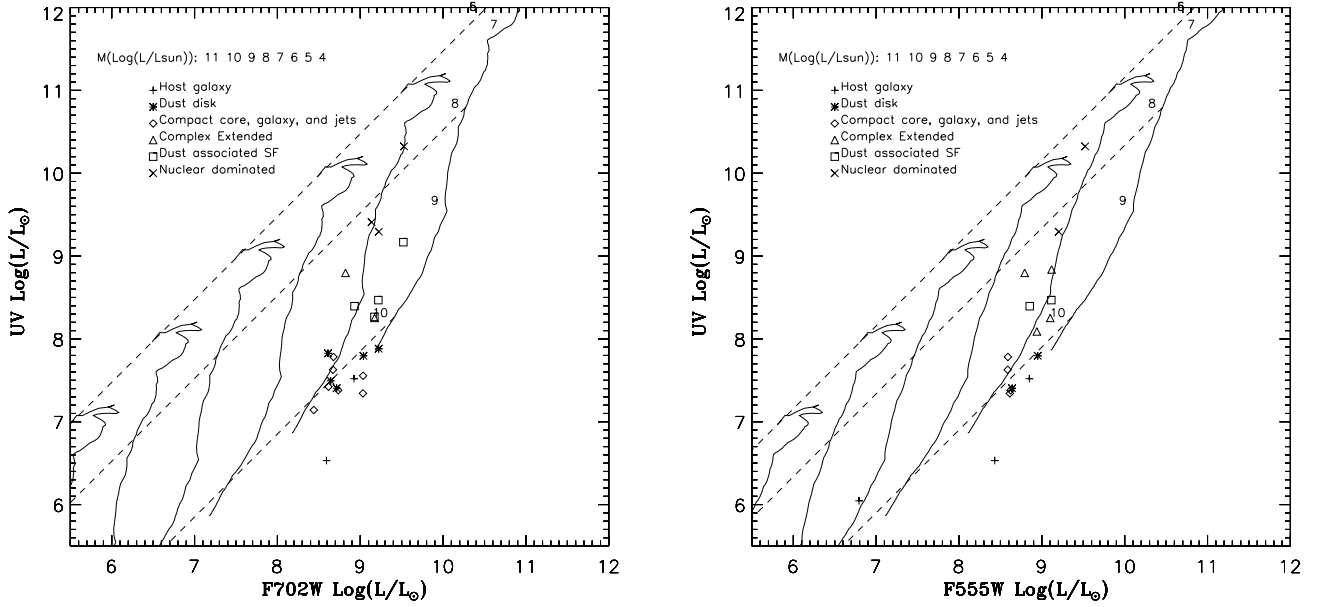Fig. 36.— Constant star formation models.
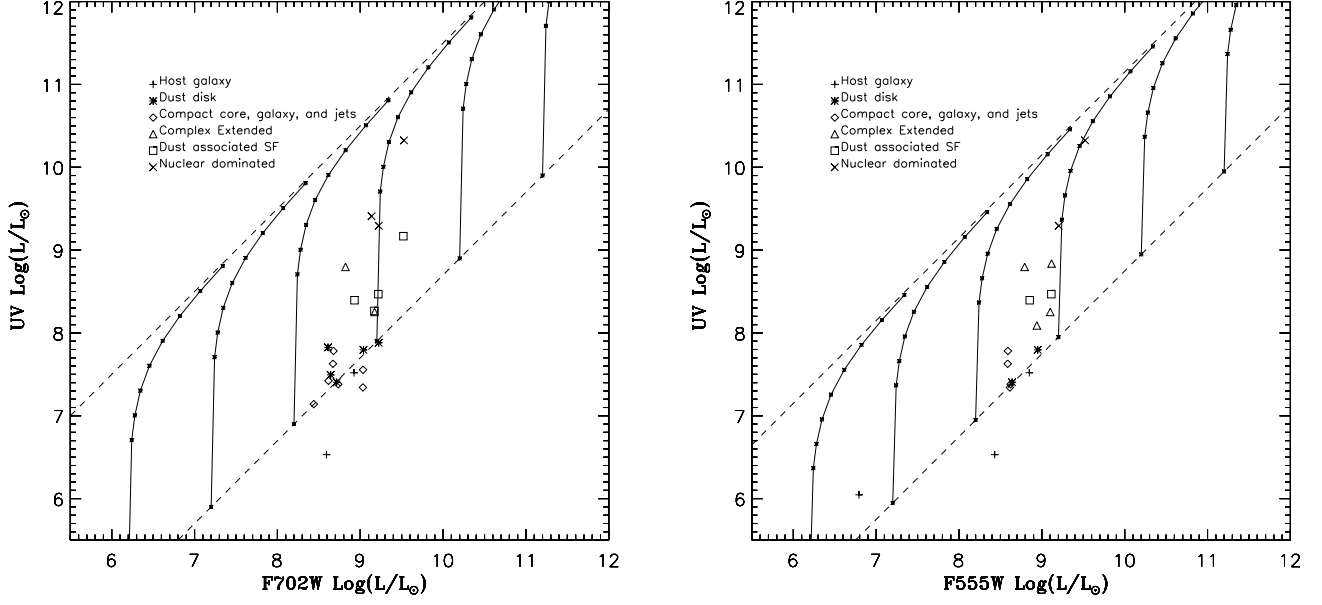

Fig. 37.— Single burst star formation models.
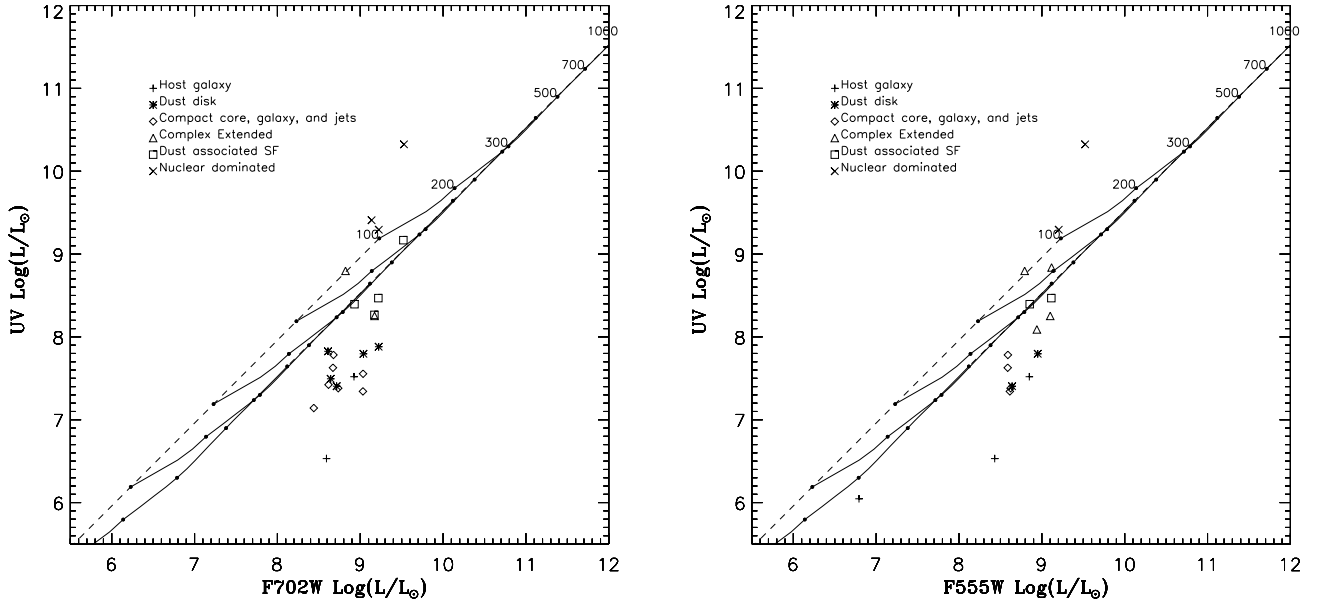
Fig. 38.— Young and Old starburst mixing models.

Fig. 39.— Shock ionization models.

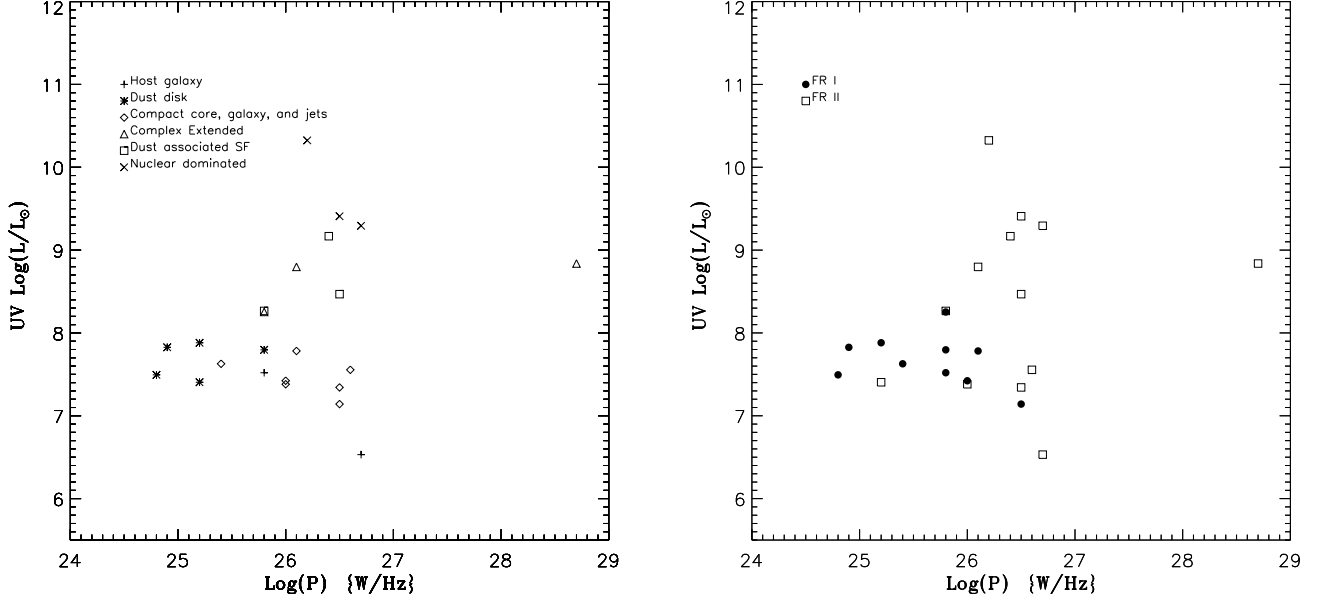Fig. 40.— UV luminosity versus total radio power.

Table 1.   Observation Log

3C	STIS Observation Date	SRF2 exposure (s)	F25CN182 (s)	F702W (s)	F555W (s)	References
	STIS NUV MAMA Observations			WFPC2 Data		
29	2000 Jun 08	1440	⋯	280	600	1,2
35	2000 Feb 23	1440	⋯	280	600	1,2
40	2000 Jun 03	1440	⋯	560	600	1,3
66B	1999 Jul 13	1440	⋯	280	460	1,2
192	2000 Mar 23	1440	⋯	⋯	600	3
198	2000 Apr 23	1440	⋯	280	600	1,2
227	2000 Jan 25	1440	⋯	560	600	1,2
231	1999 Nov 10	1440	⋯	⋯	3100	4
236	1999 Oct 05	1440	⋯	560	600	1,3
270	2000 Mar 05	1440	⋯	280	⋯	1
285	2000 Apr 16	1440	⋯	1200	600	1,2
293	2000 Jun 14	1440	⋯	280	⋯	1
296	2000 Apr 15	1440	⋯	280	⋯	1
305	2000 Apr 27	1440	⋯	560	600	1,2
310	2000 Jun 10	1440	⋯	280	⋯	1
317	1999 Jul 26	1440	⋯	280	6200	1,5
321	2000 Jun 05	1440	⋯	280	⋯	1
326	2000 Mar 12	1440	⋯	280	600	1,2
338	2000 Jun 04	1440	⋯	280	⋯	1
353	2000 Jun 22	1440	⋯	280	600	1,2
382	2000 Feb 23	⋯	1440	280	600	1,2
388	2000 Jun 02	1440	⋯	280	⋯	1
390.3	1999 Aug 10	⋯	1440	280	⋯	1
405	2000 Jun 25	2160	⋯		2700	6
449	2000 Apr 16	1440	⋯	560	⋯	1
452	2000 Jan 30	⋯	1440	280	⋯	1
465	2000 Jan 30	1440	⋯	280	600	1,2

Note. — References: HST program identification and principal investigator for F702W and F555W data: 1– GO 5476 Sparks, 2– GO 6967 Sparks, 3– GO 6348 Sparks, 4– GO 7446 O'Connell, 5– GO 6810 Geisler, 6– GO 5368 Jackson

Table 2.   Radio Properties of the STIS snapshot sample.

3C	z	S_{178}	$\log P_{178}$	α	FR	E(B-V)
29	0.0447	15.1	25.8	0.50	I	0.036
35	0.0670	10.5	26.0	0.77	II	0.141
40	0.0177	26.0	25.2	0.66	II	0.041
66b	0.0215	24.6	25.4	0.62	I	0.080
192	0.0598	21.1	$\cdots$	0.79	II	0.054
198	0.0815	9.7	26.1	0.69	II	0.026
227	0.0861	30.4	26.7	0.67	II	0.026
231	0.000677	$\cdots$	$\cdots$	$\cdots$	$\cdots$	0.159
236	0.0989	14.4	26.5	0.51	II	0.011
270	0.0073	51.8	24.8	0.51	I	0.018
285	0.0794	11.3	$\cdots$	0.95	II	0.017
293	0.0452	12.7	25.8	0.45	II	0.017
296	0.0237	13.0	25.2	0.67	I	0.025
305	0.041439	15.7	25.8	0.85	I	0.029
310	0.0540	55.1	26.5	0.92	I	0.042
317	0.0350	49.0	26.1	1.02	I	0.037
321	0.0960	13.5	26.4	0.60	II	0.044
326	0.0885	20.4	26.5	0.88	II	0.053
338	0.0298	46.9	26.0	1.19	I	0.012
353	0.0304	236.0	26.7	0.71	II	0.439
382	0.0578	19.9	26.2	0.59	II	0.070
388	0.0908	24.6	26.6	0.70	II	0.080
390.3	0.0561	47.5	26.5	0.75	II	0.071
405	0.056075	8700	28.7	0.74	II	0.381
449	0.0171	11.5	24.9	0.58	I	0.167
452	0.0811	54.4	26.9	0.78	II	0.137
465	0.0293	37.8	25.8	0.75	I	0.069

Table 3. F_λ Measurements.

3C	UV $(\text{erg s}^{-1} \text{ cm}^{-2} \text{ Å}^{-1})$	F702W $(\text{erg s}^{-1} \text{ cm}^{-2} \text{ Å}^{-1})$	F555W $(\text{erg s}^{-1} \text{ cm}^{-2} \text{ Å}^{-1})$
29	$5.272 \times 10^{17} \pm 1.1 \times 10^{18}$	$1.333 \times 10^{15} \pm 3.5 \times 10^{18}$	$1.223 \times 10^{15} \pm 3.1 \times 10^{18}$
35	$8.123 \times 10^{18} \pm 3.2 \times 10^{19}$	$3.042 \times 10^{16} \pm 1.5 \times 10^{18}$	$2.376 \times 10^{16} \pm 1.2 \times 10^{18}$
40	$2.489 \times 10^{16} \pm 1.5 \times 10^{18}$	$5.184 \times 10^{15} \pm 4.7 \times 10^{18}$	$4.762 \times 10^{15} \pm 6.1 \times 10^{18}$
66b	$2.138 \times 10^{16} \pm 1.2 \times 10^{18}$	$2.915 \times 10^{15} \pm 5.2 \times 10^{18}$	$2.550 \times 10^{15} \pm 5.2 \times 10^{18}$
192	$9.636 \times 10^{17} \pm 9.1 \times 10^{19}$	$\cdots$	$7.995 \times 10^{16} \pm 2.4 \times 10^{18}$
198	$3.228 \times 10^{16} \pm 1.4 \times 10^{18}$	$3.235 \times 10^{16} \pm 1.7 \times 10^{18}$	$3.329 \times 10^{16} \pm 1.6 \times 10^{18}$
227	$9.069 \times 10^{16} \pm 2.0 \times 10^{18}$	$7.311 \times 10^{16} \pm 1.7 \times 10^{18}$	$7.697 \times 10^{16} \pm 2.4 \times 10^{18}$
231	$3.250 \times 10^{15} \pm 5.4 \times 10^{18}$	$\cdots$	$3.266 \times 10^{14} \pm 8.1 \times 10^{18}$
236	$5.667 \times 10^{17} \pm 8.1 \times 10^{19}$	$4.556 \times 10^{16} \pm 1.4 \times 10^{18}$	$3.705 \times 10^{16} \pm 1.7 \times 10^{18}$
270	$2.120 \times 10^{15} \pm 3.4 \times 10^{18}$	$2.718 \times 10^{14} \pm 1.7 \times 10^{17}$	$\cdots$
285	$1.435 \times 10^{16} \pm 9.6 \times 10^{19}$	$4.466 \times 10^{16} \pm 9.7 \times 10^{19}$	$4.144 \times 10^{16} \pm 1.9 \times 10^{18}$
293	$3.291 \times 10^{16} \pm 2.2 \times 10^{18}$	$2.397 \times 10^{15} \pm 5.1 \times 10^{18}$	$\cdots$
296	$4.668 \times 10^{16} \pm 1.6 \times 10^{18}$	$9.637 \times 10^{15} \pm 8.2 \times 10^{18}$	$\cdots$
305	$3.490 \times 10^{16} \pm 1.4 \times 10^{18}$	$2.787 \times 10^{15} \pm 3.4 \times 10^{18}$	$2.599 \times 10^{15} \pm 4.5 \times 10^{18}$
310	$1.448 \times 10^{17} \pm 3.2 \times 10^{19}$	$2.949 \times 10^{16} \pm 1.5 \times 10^{18}$	$\cdots$
317	$1.563 \times 10^{16} \pm 1.2 \times 10^{18}$	$1.225 \times 10^{15} \pm 3.9 \times 10^{18}$	$1.097 \times 10^{15} \pm 1.1 \times 10^{18}$
321	$4.798 \times 10^{16} \pm 1.6 \times 10^{18}$	$1.120 \times 10^{15} \pm 3.1 \times 10^{18}$	$\cdots$
326	$7.919 \times 10^{18} \pm 3.2 \times 10^{19}$	$4.205 \times 10^{16} \pm 1.8 \times 10^{18}$	$1.727 \times 10^{16} \pm 1.0 \times 10^{18}$
338	$1.127 \times 10^{16} \pm 9.6 \times 10^{19}$	$1.556 \times 10^{15} \pm 4.2 \times 10^{18}$	$\cdots$
353	$7.511 \times 10^{19} \pm 4.3 \times 10^{19}$	$5.578 \times 10^{16} \pm 2.0 \times 10^{18}$	$3.109 \times 10^{16} \pm 1.5 \times 10^{18}$
382	$2.594 \times 10^{14} \pm 3.4 \times 10^{17}$	$2.970 \times 10^{15} \pm 4.6 \times 10^{18}$	$3.127 \times 10^{15} \pm 4.4 \times 10^{18}$
388	$1.013 \times 10^{17} \pm 5.2 \times 10^{19}$	$3.776 \times 10^{16} \pm 1.8 \times 10^{18}$	$\cdots$
390.3	$3.320 \times 10^{15} \pm 1.3 \times 10^{17}$	$1.278 \times 10^{15} \pm 3.0 \times 10^{18}$	$\cdots$
405	$6.536 \times 10^{17} \pm 6.0 \times 10^{19}$	$\cdots$	$5.255 \times 10^{16} \pm 8.6 \times 10^{19}$
449	$2.906 \times 10^{16} \pm 1.9 \times 10^{18}$	$3.317 \times 10^{15} \pm 3.7 \times 10^{18}$	$\cdots$
465	$1.834 \times 10^{16} \pm 1.6 \times 10^{18}$	$3.753 \times 10^{15} \pm 5.7 \times 10^{18}$	$3.264 \times 10^{15} \pm 5.0 \times 10^{18}$

Table 4.   Luminosity Measurements.

3C	NUV log(L/L$_\odot$)	F702W log(L/L$_\odot$)	F555W log(L/L$_\odot$)
29	7.520 ± 0.12	8.924 ± 0.04	8.849 ± 0.05
35	7.380 ± 0.45	8.734 ± 0.14	8.623 ± 0.18
40	7.404 ± 0.13	8.715 ± 0.04	8.641 ± 0.05
66B	7.628 ± 0.25	8.670 ± 0.08	8.588 ± 0.10
192	8.090 ± 0.17	⋯	8.940 ± 0.07
198	8.797 ± 0.08	8.822 ± 0.03	8.792 ± 0.04
227	9.294 ± 0.08	9.224 ± 0.03	9.204 ± 0.03
231	6.046 ± 0.49	⋯	6.793 ± 0.20
236	8.468 ± 0.35	9.218 ± 0.11	9.114 ± 0.14
270	7.494 ± 0.06	8.643 ± 0.02	⋯
285	8.395 ± 0.06	8.931 ± 0.02	8.853 ± 0.02
293	8.266 ± 0.06	9.171 ± 0.02	⋯
296	7.882 ± 0.08	9.222 ± 0.02	⋯
305	8.253 ± 0.09	9.172 ± 0.03	9.101 ± 0.04
310	7.141 ± 0.14	8.439 ± 0.04	⋯
317	7.782 ± 0.12	8.676 ± 0.04	8.590 ± 0.05
321	9.167 ± 0.14	9.520 ± 0.04	⋯
326	7.342 ± 0.18	9.032 ± 0.05	8.613 ± 0.07
338	7.423 ± 0.04	8.617 ± 0.01	⋯
353	6.531 ± 1.55	8.592 ± 0.42	8.431 ± 0.56
382	10.324 ± 0.22	9.528 ± 0.07	9.523 ± 0.09
388	7.555 ± 0.27	9.034 ± 0.08	⋯
390.3	9.409 ± 0.22	9.137 ± 0.07	⋯
405	8.838 ± 1.14	⋯	9.117 ± 0.49
449	7.826 ± 0.51	8.610 ± 0.16	⋯
465	7.796 ± 0.22	9.039 ± 0.07	8.950 ± 0.09